

## Brachytherapy Needle Steering Guidance Using Image Overlay

Carlos Rossa, McNeil Keri, Mahdi Tavakoli  
University of Alberta, Edmonton, Canada  
carlos.rossa@uoit.ca; mcniel@ualberta.ca; mahdi.tavakoli@ualberta.ca

**Abstract** - This paper presents a physical simulator for needle steering in brachytherapy. As the user inserts the needle in a phantom tissue, images of the needle and prostate shape reconstructed from 2D transverse ultrasound images are displayed online in a semi-transparent mirror. During insertion, the user sees the images as if they were floating inside the phantom accounting for scale and orientation. The ultrasound images of the needle are combined with a needle-tissue interaction model that predicts the needle deflection further along the insertion process. The necessary manoeuvres that bring the needle towards its intended target location are displayed to the user along with the actual needle location. This platform allows the user to test different manual and robotic assisted needle steering techniques. Reported experimental results confirm the accuracy of the system in reconstructing and overlaying images onto the phantom.

### I. MOTIVATION

Percutaneous needle insertion is a widespread minimally invasive surgical intervention. Applications of needle insertion include brachytherapy cancer treatment, tissue biopsy sampling, neurosurgery, radio-frequency ablation, and drug delivery. In brachytherapy, for instance, needles loaded with tiny radioactive seeds are inserted in the patient's prostate. Once the needles are fully inserted, the needles are pulled back to permanently leave the seeds in their desired destinations. As a consequence, controlling the radiation dose that will destroy cancer cells without affecting adjacent healthy tissues critically depends on the accurate guidance of the needle towards a body target.

Due to the lack of sufficient feedback during insertion and the limited steerability of needles, needle placement during brachytherapy is usually planned with needles assumed to follow a straight-line trajectory. In practice, this assumption does not hold true as the needle deviates from this path. For a comprehensive survey on issues related to needle steering, see Rossa (2017). In turn, inserting and retracting needles in tissue causes the tissue to move and deform, posing a strong risk of inadvertent target misses. To deal with these challenges, ultrasound images of the needle within the tissue are typically used to guide the needle towards the target. Ultrasound images often contain artifacts that are hard to identify and distinguish from targets and needles. In addition, to view the ultrasound images, the surgeon must look away from the patient and towards a monitor while manoeuvring the needle, introducing an additional challenge in interpreting the images.

In order to improve the visualization of needles and targets during clinical interventions, augmented reality (AR) has been the focus of significant research. Image processing combined with augmented reality has the ability to project onto real world images, reconstructed images of the inner body acquired from any medical imaging modality Weiss (2011). An augmented reality display adds an extra layer of virtual information on top of the perception of the real world in real time, making many surgical tasks simpler and safer for the surgeon. The simplest AR system consists of a semitransparent mirror through which the viewer looks directly at the patient Nikou (2000). An image is projected onto the mirror by a standard monitor so that the viewer simultaneously sees a reflection of the computer display that appears with correct orientation and scale and the real world image Blackwell (2000). In brachytherapy, this can be used as a training environment to help user

develop needle steering skills based on the ability to visualize needles and anatomical structures within the tissue in an intuitive way.

Related applications of AR for needle insertion guidance include arthrography Fichtinger (2005), Westwood (2006), ultrasound guided needle placement training Magee (2007), Zhu (2006), surgical laparoscopy Wacker (2005), magnetic resonance image guided biopsy Wacker (2006), liver puncture Nicolau (2005) and ablation Nicolau (2009), Teber (2009), and computed tomography Stetten (2001), Stetten (2001b), Sauer (2002). In Fischer (2007), the AR system identifies the optimal needle insertion path such that the surgeon can follow a desired needle insertion trajectory under the assumption that the needle will remain unbent during insertion. This chapter introduces the first implementation of an AR system for skills development for brachytherapy needle steering. The system displays reconstructed images of the actual shape of a needle in the tissue, as well as the location of the prostate phantom and the target locations in real time. In addition to measuring the actual needle deflection, ultrasound image processing is combined with a needle-tissue physical model Rossa (2016) that predicts the needle deflection further along the insertion process. The necessary manoeuvres that bring the needle towards its intended target location are then displayed to the user online.

This chapter is structured as follows. After we get acquainted with the proposed physical system in Section II, we will see how several transverse ultrasound images are combined to reconstruct the actual 3D shape of a prostate phantom embedded in a synthetic tissue. Next, the needle-tissue model presented in Rossa (2016) is used to predict needle deflection during the insertion process. Once we have reconstructed the prostate geometry and the needle trajectory, we will proceed with image registration to ensure the prostate and needle will appear to the user with correct orientation and scale floating inside the patient. Finally, in Section IV, experimental results confirm the ability of the proposed system in overlaying the reconstructed images.

## II. THE AUGMENTED REALITY SYSTEM

The augmented reality system for needle steering training is schematically depicted in Fig. 1. The system is composed of a tissue phantom that embeds a synthetic prostate phantom. Whilst the user inserts an 18-gauge, 200 mm long, brachytherapy needle through a standard brachytherapy template grid, an ultrasound probe acquires 2D images of the tissue, in a plane normal to the straight needle (the  $(x, y)$  plane of Fig.1). A linear stage connected to a stepper motor by a belt-pulley mechanism controls the position of the ultrasound probe such that it slides back and forth above the tissue (along  $z$ ). Template grids consist of equidistant rows and columns of holes spaced 5 mm apart. In prostate brachytherapy, the needle is inserted through a hole and the corresponding position is marked on an overly in the calibrated ultrasound image, which corresponds to a target location in the prostate. These transverse ultrasound images show a cross section of an object inside the tissue. By combining several transverse images acquired at different positions, the 3D volume of the objects can be reconstructed. This simulates an operating room setup where a transrectal ultrasound probe is placed below the pelvic tissues of interest. The techniques presented here can be employed in the clinical context, as they only require the current position of the ultrasound probe.

As the user inserts the needle, we combine the 2D ultrasound images of the needle and of the target and reconstruct their 3D images, adjust their magnification, appropriately rotate the images and then render them on a monitor placed above the tissue phantom. These images are reflected in the semitransparent mirror located between the user and the phantom. The user sees the images generated by the monitor as if they were floating behind the mirror in the so-called projection plane. The goal of the system is to match the projected image and the real objects inside the phantom with the user's viewpoint such that they appear to the user to be inside the phantom with proper location

and size.

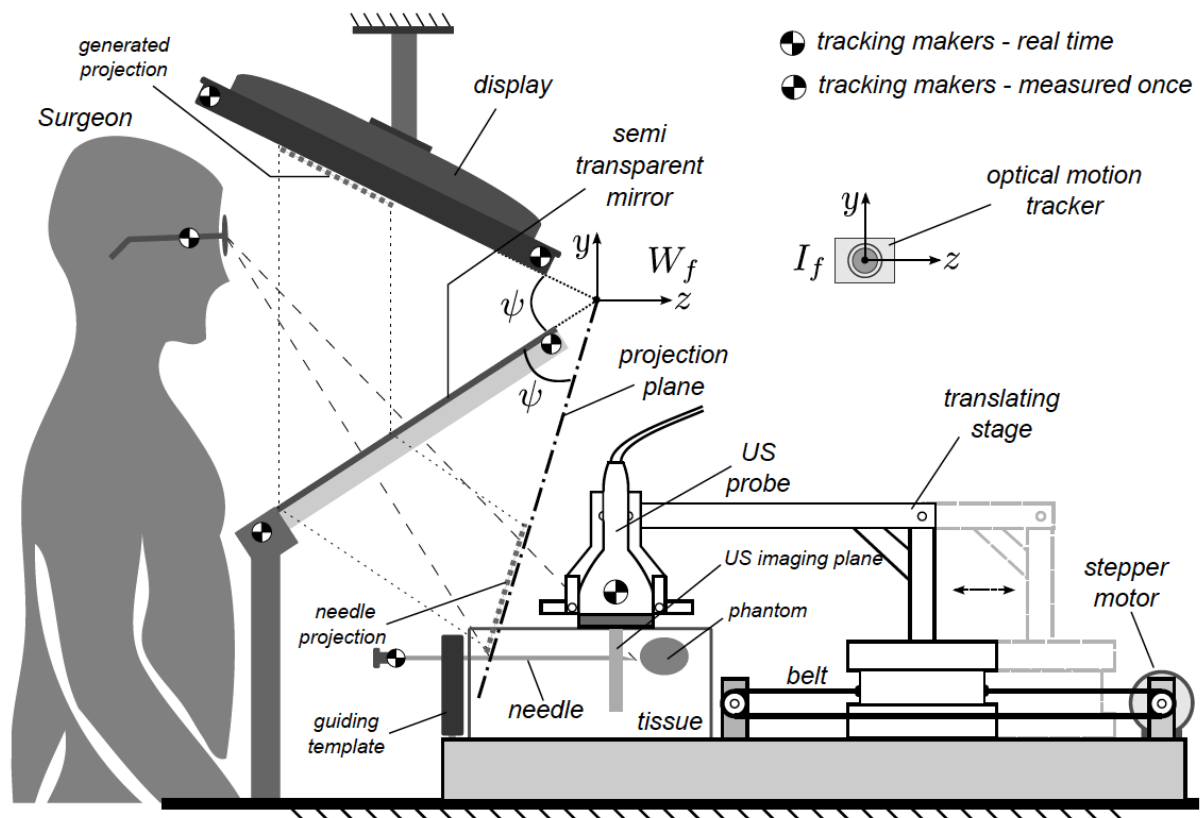


**Figure 1 - The training system.** As the user inserts a needle into a phantom, an ultrasound probe moves above the tissue to acquire 2D images. The reconstructed images of the needle and of a prostate phantom embedded in the tissue are displayed in the monitor and reflected in the semi-transparent mirror. The images will then appear to the user to be floating inside the tissue with proper size and location. A motion tracker measures the position of the mirror, the monitor, the needle base, and the user's eyes.

To this end, one needs to generate the images to be displayed to the user, and then calculate their position in the monitor. We begin by placing the images obtained in the ultrasound frame in the real world frame. In other words, we need to calculate their relative position in the setup. Next, we calculate the image points in the projection plane by tracing a straight line from the user's eye to a particular point in the image, called a perspective line. Notice that as shown in Fig. 1, the image in the projection plane has the same size as it appears in the monitor. Therefore, the corresponding points in the monitor image are found when the perspective lines intercept the projection plane.

To perform these steps, one needs to measure the position of the user's eyes, of the needle base, and of the ultrasound probe online. As well, the orientation of the mirror and of the display must be known. Tracking markers are placed in each of the above referenced objects whose position is measured at by an optical motion tracker placed on the side of the setup. In order to measure the position of the user's eyes, the user wears glasses without lenses that are equipped with two tracking markers on the right side.

In the following, we describe the three parts that constitute the augmented reality system, i.e., 1) the ultrasound-based reconstruction of the target and prostate phantom, 2) estimation of future needle deflections, and 3) the rigid body transformation that generates the images of 1) and 2) in the display.

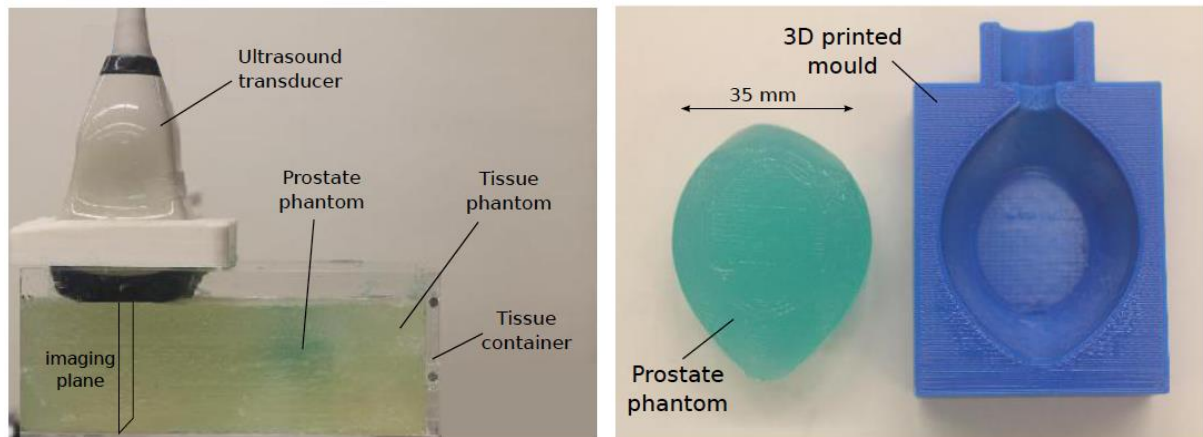


**Figure 2 - Fig. 2. Tissue phantoms. The prostate phantom in (right), fabricated using a 3D printed mould is embedded in the phantom tissue shown in the right. Both tissues are made of plastisol gel with different stiffness.**

### A. Segmentation of Prostate Phantom

The first step in running the augmented reality system is to scan the tissue phantom with the ultrasound probe. The tissue phantom used in the setup is made of plastisol gel (M-F Manufacturing, Fort Worth, USA) with a volume ratio of four parts of plastisol to one part of plastic softener (see Fig. 2(a)). To simulate the target location, we embedded in this tissue a prostate phantom fabricated with a custom made 3D printed mould (see Fig. 2(b)), using a mixture with a higher concentration of plastisol i.e., 6 to 1. In order to mimic the ultrasound imaging characteristics of a human prostate, 10 grams of silica gel are added into the 0.5 litre mixture during fabrication of the prostate phantom.

The ultrasound probe is controlled to slide above the tissue phantom while acquiring successive transverse images at every 0.15 millimetres increment. Each image will show a cross section of the prostate phantom. The image processing sequence used to find the contour of the prostate for each of the acquired transverse images is shown in Fig. 3. First, the original image shown in (a) is filtered using a 2D Gaussian low pass filter and results in the image (b). The generated kernel is then convolved with the original image in order to sharpen the edges of the object in the image. After stretching the pixel intensity range in the gray scale to 0 to 255, a 45% image thresholding generates the binary image seen in (c). In the next step, we find the centroid of each of the white regions shown in (c) using the Matlab function *regionprops*. An elliptically shaped morphological structuring element is then created to fit each of these regions in order for one to calculate their approximate area. The biggest area is assumed to correspond to the prostate shape and the other regions are discarded. The result is shown in (d). Next, the Matlab function *bwperim* returns the contour of the retained image (see (e)), which is converted into polar coordinates and interpolated in order to close the contour. The final result overlaid with the original image is shown in (f). On a 6 GB of RAM with Intel Core i3 3.3 GHz computer, the processing time for each of the ultrasound images is 85 milliseconds.

By combining the successive prostate contours with the corresponding measured position of the ultrasound probe, the 3D volume of the prostate phantom is reconstructed.

### B. Estimating Future Needle Deflection

Once the prostate phantom is found using the steps described in the previous section, the ultrasound probe moves back to the point where the needle enters the tissue and is controlled to follow the

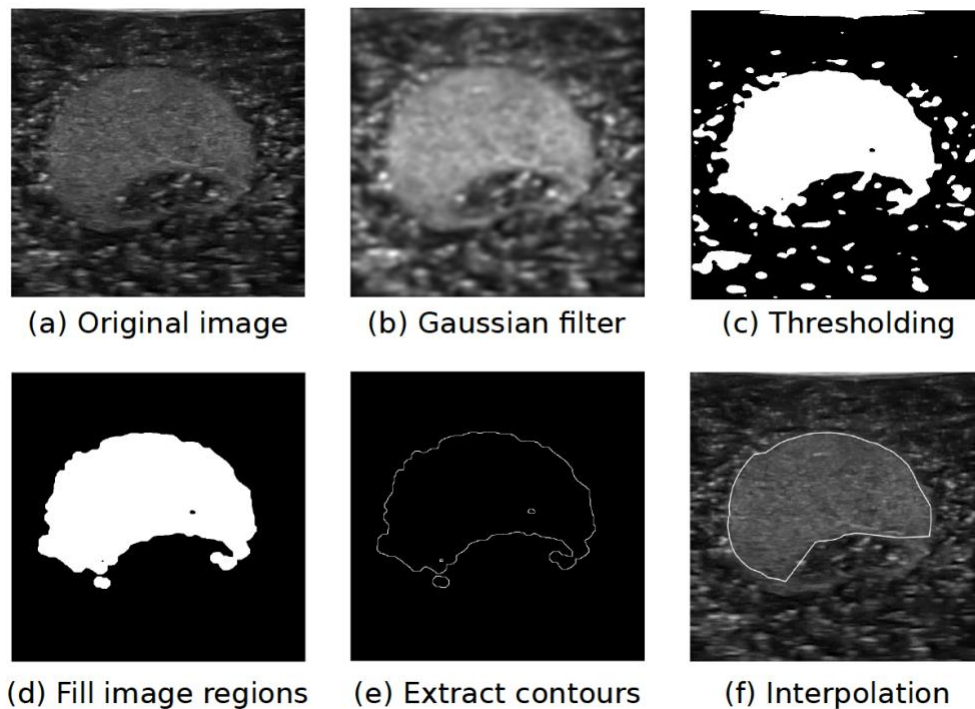


**Figure 3 - Image processing steps used to segment the prostate phantom. (a) Original transverse image, (b) filtered image using a 2D Gaussian low pass filter, (c) binary image after convolution and thresholding, (d) obtained contours after filling the small white regions in the image, (e) extracted contour, and (f) interpolated contour on the original image (only used for visual verification).**

position of the needle tip as the needle is inserted. In each of the ultrasound images, the needle tip appears as a bright spot along with extraneous background objects. To remove the majority of these objects, we first define a region of interest (ROI) that limits the search for the needle to a small section of the image (see Fig. 4(a)), initially located at the needle’s entry point in the tissue. The ROI consists of a square with a width of 5 times the needle radius. In frame  $f$ , the ROI is centred on the position of the needle found in frame  $f - 1$ . Therefore, as the needle moves transversely in successive ultrasound images, the ROI moves such that the needle tip will always be located in the ROI. The Matlab function *imadjust* applies an intensity transformation to the image to improve the visibility of bright points. Next, we use an intensity threshold to obtain a set of candidate pixels for the needle within the axial image. Finally, a Kalman filter is used to predict which of the candidate pixels represent the actual needle tip within the ROI, given the needle’s historical trajectory, similar to Zhao (2012).

The measured needle deflection is then used in a mechanical model of the needle-tissue system that calculates the future needle tip deflection, given the past positions of the needle tip Rossa (2016). Two cases are considered. In the first case, the model calculates the needle deflection as the user inserts it until a desired depth in the tissue. In the second case, the deflection is calculated considering that the user rotates the needle base by 180 around its shaft, at the current insertion depth, with the aim of reversing the direction of the needle deflection. Both cases are then displayed to the user. An example is shown in Fig. 4(b). Combined, the image processing and the needle deflection estimation are performed in less than 60 milliseconds on a 6 GB of RAM with Intel Core i3 3.3 GHz computer.

Now that images have been acquired and processed, the objective is to find their position in the monitor such that their projection will match the user’s view of the real objects. This is described in the next section.

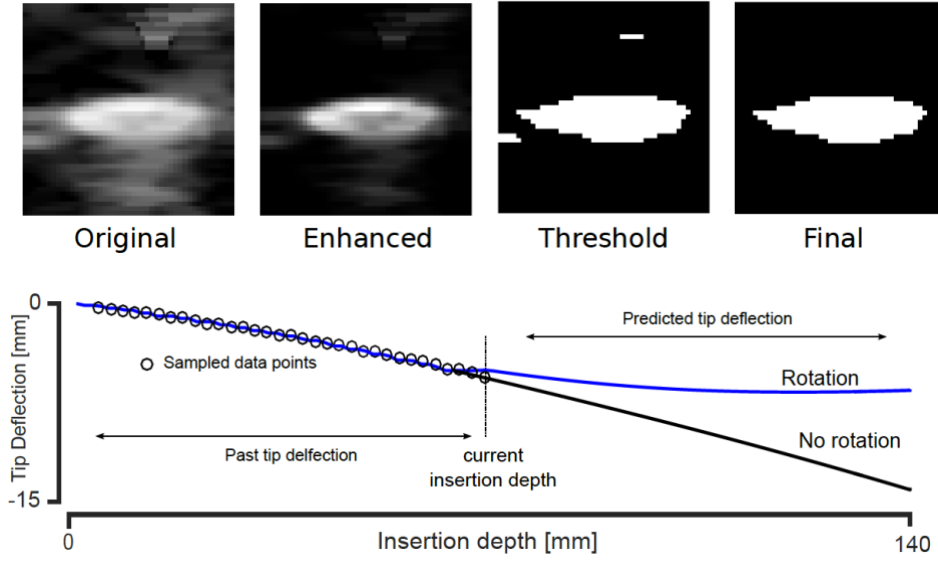


**Figure 4 - Fig. 4. Image processing and needle deflection estimation. In the first figure, the different steps used to find the needle tip in each transverse image. In second figure, the obtained deflection is used in a model to predicted future deflections of the needle tip as the needle is inserted and rotated at the current depth.**

### III. IMAGE REGISTRATION

In the following,  $M^N$  defines a column vector  $M$ , which has coordinates  $m_x^N$ ,  $m_y^N$ , and  $m_z^N$  along the  $x$ ,  $y$ , and  $z$  axes, respectively, as expressed in the frame  $N$ . The frame  $I_f$  is the frame of the optical tracker. To determine the relative position of the semi-transparent mirror and of the display shown in Fig. 1, we place  $i$  tracking markers on the side of each object whose position  $P_i$  is measured by the motion tracker in the frame  $I$ . The point  $P_1$  will be considered to be the origin of the display frame, called  $D_f$  (see Fig. 5).

The 3D equations of the semi-transparent mirror and of the display planes can be written as  $y = m_m^I z + b_m^I, \forall x$  and  $y = m_d^I z + b_d^I, \forall x$ , respectively, where  $m_d^I$  and  $m_m^I$  are the plane slopes, and  $b_m^I$  and  $b_d^I$  are the intersection points of each plane with the  $y^I$  axis. As functions of the tracking markers position  $P_i^I$ ,  $m$  and  $b$  are computed as follows:

$$\begin{aligned} m_d^I &= \frac{p_{2y}^I - p_{1y}^I}{p_{1z}^I - p_{2z}^I}, & b_d^I &= p_{2y}^I - p_{2z}^I m_d^I, \\ m_m^I &= \frac{p_{4y}^I - p_{3y}^I}{p_{3z}^I - p_{4z}^I}, & b_m^I &= p_{4y}^I - p_{4z}^I m_m^I, \end{aligned} \quad (1)$$

For convenience, we will define a second frame, called the world frame  $W_f$ , whose origin coincides with the intersection of the mirror and display planes, as shown in Fig. 5. We assume that the two planes are not rotated with respect to each other around  $z$  and  $y$ , and that the coordinate of the world frame along  $x$  is arbitrarily chosen to be  $p_{1x}^I$ . By setting the equations of the mirror and display planes to be equal, one finds the position of the world frame, as expressed in the motion tracker frame, as

$$W_f^I = \begin{bmatrix} p_{1x}^I & \frac{b_m - b_d}{m_b - m_m} & \frac{m_d b_m - m_m b_d}{m_d - m_m} \end{bmatrix}^T. \quad (2)$$

Thus, the coordinates of the tracking markers in the world frame are calculated as  $P_1^W = P_1^I - W_f^I$ ,  $P_2^W = P_2^I - W_f^I$ ,  $P_3^W = P_3^I - W_f^I$ , and  $P_4^W = P_4^I - W_f^I$ . With the world frame and the reference points defined, we can proceed with the registration of the processed ultrasound images.

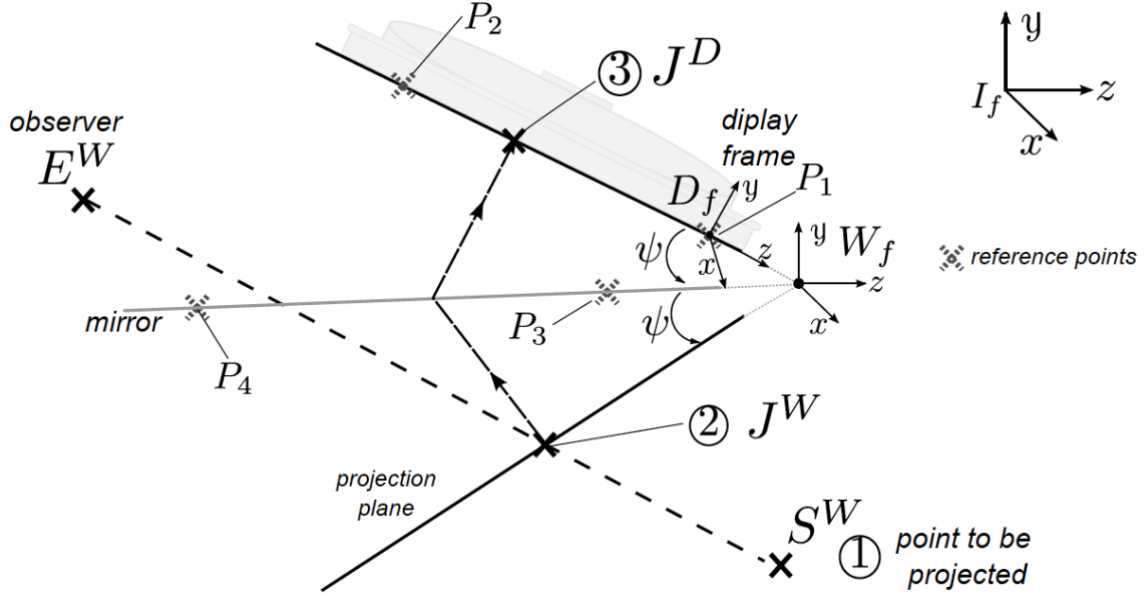


**Figure 5 - Rigid transformations.** The point  $S^W$  obtained from ultrasound images is found in the projection plane as a point  $J^W$ , which corresponds to the intersection of a line connecting the observer's eye  $E^W$  to  $S^W$ . Dashed crosses indicate known points measured by the optical tracker. If  $I_f$  and  $W_f$  are the origins of the motion tracker frame and world frame, respectively.

The ultrasound probe acquires 2D images (in the  $(x, y)$  plane) that are to be express in the 3D world frame. Let us begin the image registration by scaling the ultrasound images. The 2D ultrasound image frame  $U_f$  is located at the upper-right corner of the ultrasound imaging plane such that it is always parallel to the  $(x, y)$  plane in  $W_f$ . A point  $S^U$  in an ultrasound image has coordinates  $s_x^U$  and  $s_y^U$  in pixels along the  $x$  and  $y$  axes, respectively. The number of pixels in each axis is  $px_{Ux}$  and  $px_{Uy}$ . Let  $v_{Ux}$  and  $v_{Uy}$  be the ultrasound image field of view in meters along each axis, respectively. The number of pixels and the field of view size are constant and are known from the ultrasound machine settings. The scaling factor in  $x$  and  $y$  that converts a point from pixels to meters is given by  $f_{Ux} = v_{Ux}/px_{Ux}$  and  $f_{Uy} = v_{Uy}/px_{Uy}$ .

Now that the magnification ratios of the image are known, the points in the ultrasound frame can be translated to the world frame. The 3D position of the ultrasound probe measured by the optical tracker is  $R^I = [r_x^I \ r_y^I \ r_z^I]^T$ , which can be expressed in the world frame as  $R^W = R^I - W_f^I$ . In the setup,  $R^I$  is only measured once. When the probe moves, its location along  $z$  with respect to  $p_z^W$  is measured by a potentiometer in real time, and it is called  $p_0$ . Finally, the position  $S^W$  in the world frame of a point  $S^U$  is given by:

$$S^W = \begin{bmatrix} f_{Ux} & 0 & 0 \\ 0 & f_{Uy} & 0 \\ 0 & 0 & 0 \end{bmatrix} \cdot \begin{bmatrix} s_x^U \\ s_y^U \\ 0 \end{bmatrix} + \begin{bmatrix} r_x^W \\ r_y^W \\ r_z^W \end{bmatrix} + \begin{bmatrix} 0 \\ 0 \\ p_0 \end{bmatrix} \quad (3)$$

Having converted the ultrasound point to the world frame, the next step is to calculate where the projection plane is. Let us call  $\gamma$  the angle between the display and mirror planes with respect to  $x^W$ . The projection plane will appear to the user to be floating behind the mirror, rotated from the mirror plane around  $x^W$  by  $\psi$ . The angle  $\psi$  is:

$$\psi = \arctan \left| \frac{m_d^W - m_m^W}{1 + m_d^W m_m^W} \right| \quad (4)$$

where  $m_d^W$ , and  $m_m^W$  are calculated by inserting the reference points  $P_i^W$  in (1). Now, the projection plane is obtained by rotating the display plane by  $2\psi$  degrees clockwise about the axis  $x^W$ . The rotation matrix is

$$\mathcal{R}_x = \begin{bmatrix} 1 & 0 & 0 \\ 0 & \cos(2\psi) & \sin(2\psi) \\ 0 & 0 - \sin(2\psi) & \cos(2\psi) \end{bmatrix} \quad (5)$$

The coordinates of the rotated points are then given by  $\mathcal{R}_x P_1^W$  and  $\mathcal{R}_x P_2^W$ . As for the mirror and for the display, the projection plane can be expressed as a first order polynomial in the form  $y = m_p^W z + b_p^W$  where  $m_p^W$  and  $b_p^W \forall x$ , are given as functions of the rotated points as

$$m_p^W = \frac{\sin(2\psi) (P_{2y}^W - P_{1y}^W)}{\cos(2\psi) (P_{1y}^W - P_{2y}^W) + \sin(2\psi) (P_{1z}^W - P_{2z}^W)} \quad (6)$$

$$b_p^W = -\sin(2\psi) P_{1y}^W + \cos(2\psi) P_{1z}^W - m_p^W (\cos(2\psi) P_{1y}^W + \sin(2\psi) P_{1z}^W)$$

The parametric equation of the perspective line  $\ell(t)^W$  that connects the observer's eye  $E^W$  to a point  $S^W$  in the ultrasound image is:

$$\ell(t)^W = [te_x + s_x(1-t) \quad te_y + s_y(1-t) \quad te_z + s_z(1-t)]^T \quad (7)$$

After straightforward manipulation, we find that the perspective line  $\ell^W$  intercepts the projection plane  $y = m_p^W z + b_p^W$  when  $t = t_p$ , where  $t_p$  is

$$t_p = \frac{s_y^W - m_p^W s_z^W - b_p^W}{m_p^W (e_z^W - s_z^W) + s_y^W - e_y^W} \quad (8)$$

Thus, the point that must be generated in the projection plane in order to match the user's angle of view with the actual point seen in the ultrasound image is  $J^W = \ell(t_p)^W$ .

The last transformation will convert the point  $J^W$  found in the projection plane (world frame) to the display frame. As for the ultrasound images, let  $px_{Dx}$  and  $px_{Dz}$  be the number of pixels in the  $x$  and  $z$  axes of the display, and  $v_{Dx}$  and  $v_{Dz}$  be the display image field of view in meters along each axis. The scaling factor in  $x$  and  $z$  is given by  $f_{Ux} = v_{Ux}/px_{Ux}$  and  $f_{Uz} = v_{Uz}/px_{Uz}$ . The display and monitor are only rotated around  $x$ , and therefore have the same scaling. In order to convert a point

from the projection plane to the display frame, one simply accounts for the distance between the display and the origin of the world frame. As is has been defined, this distance is  $J^W - \mathcal{R}_x P_1^W$ . Thus, the coordinates of a point  $J^W$  in pixels, in the display frame is:

$$J^D = \begin{bmatrix} 1/f_{Dx} & 0 & 0 \\ 0 & 0 & 0 \\ 0 & 0 & 1/f_{Dz} \end{bmatrix} \cdot (J^W - \mathcal{R}_x P_1^W) \quad (9)$$

#### IV. HARDWARE IMPLEMENTATION AND RESULTS

The prototype of the system is shown in Fig. 6(a). A 4DL14-5/38 linear 4D ultrasound probe connected to a Sonix Touch ultrasound machine (Ultrasonix, Richmond, CA) is linked to a linear stage motorized by a stepper motor. A linear potentiometer (LP-250FJ from Midori Precisions, Tokyo, JP) measures the absolute position of the ultrasound probe in real time. The semi-transparent mirror is made of a 5 mm thick standard piece of glass covered by a 40% reflective tint film. Two computers running Matlab in xPC real-time mode are used in the setup. Computer 2 receives measurements via UDP of the current position of the ultrasound probe, and uses a digital PID regulator in order to control the horizontal position of the ultrasound-imaging plane. The first computer runs the image processing and rigid transformation software. As the first computer moves the ultrasound probe; images generated in the ultrasound machine are captured by a frame grabber and sent to Computer 1 (host), where they are processed. In addition, Computer 1 receives real-time measurements of tracking markers from the optical motion tracker (BB2-BW-Hx60 from Claron Tech, Toronto, CA) and generates the desired projection of the objects that are displayed in the monitor (see 6(b)).

For simplicity, the needle is attached to a second linear stage that rotates the needle base such that the deflection only occurs on the  $(z, y)$  plane. Notice that the needle enters the tissue on the right side of the container as shown in Fig. 6(a), while the user looks at the tissue from the left side. In a different configuration, tracker markers connected to the needle base would allow the user to be in charge of the needle insertion. Notice also that the image registration routine is independent from the needle’s entry point in tissue. Thus, inserting the needle on the same side as the mirror can be performed with only minor changes in the needle physical model. In the current configuration, the user is able to manually control the needle insertion robot based on the visual feedback received from the augmented reality display.

##### A. Experimental Results

An example of the images seen by the user through the mirror is shown in Fig. 7(a). After the ultrasound probe has scanned the tissue and the image of the prostate is reconstructed, a horizontal cross section of the phantom volume, in the  $(x, z)$  plane placed at the same height along  $y$  as the needle’s base, is displayed to the user (see Fig. 7(a)). The needle is then inserted to 5 mm in the phantom tissue. Based on the measured needle deflection by the ultrasound probe, future needle deflections are calculated using Rossa (2016). In Fig. 7(b), the line projected to the left shows the predicted future deflection of the needle tip if it is further inserted to reach a depth of 150 mm. The user can reverse the direction of the deflection by rotating the needle base by 180degrees at the current depth. The curved line projected to the right indicates the resultant path. In Fig. 7(c), the insertion is carried out until the needle reaches 40% of the desired insertion depth. The updated estimation of the needle deflection, based on the historical position of the tip and of the online-estimated local mechanical properties of the tissue, indicates to the user that the needle must be rotated at the current depth in order for the needle to reach the target. Please see the enclosed video for the complete insertion.

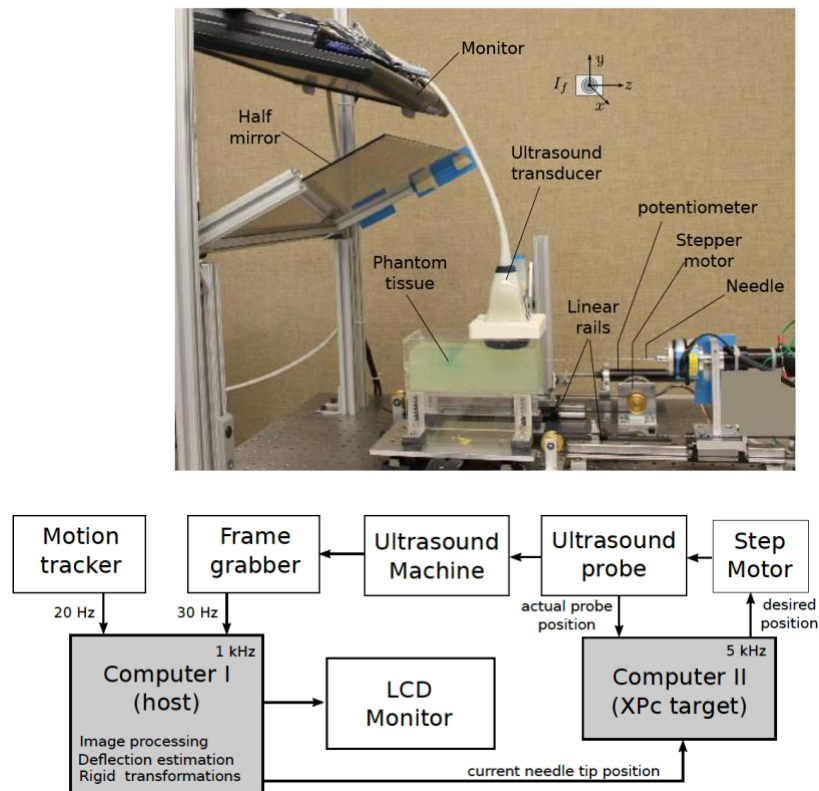


**Figure 6 - Prototype of the augmented reality system for needle insertion. In the top figure, the implementation of the system is shown with our existing needle insertion robot. The needle and the ultrasound probe are connected to two independent linear stages. Two computers are used to run the setup as depicted in the second figure. The user looks at the phantom tissue through the mirror from the left side and controls the needle insertion robot based on the provided visual feedback.**

During insertion, the position of the user's head might change. In order for the images to match the user's viewpoint, the projected images are recalculated given the current position of tracker markers connected to glasses that the user wears. Fig. 7(d) shows the adjusted images when the user's head moves to the right by approximately 200 mm as compared to the position of Fig. 7(b). This demonstrates that the system is able to automatically compensate for the position of the user's head online.

## V. DISCUSSION AND CONCLUDING REMARKS

In this paper we present the first implementation of an augmented reality system for skills development in needle steering during brachytherapy. As the needle is inserted, an ultrasound probe follows the needle tip to measure its deflection. This information is used in a needle-tissue interaction model that calculates the future needle tip deflection given the current and past measurements, and updated local mechanical properties of the phantom (Rossa (2016)). The system then displays the predicted needle tip deflection considering two cases. In the first case, the user keeps inserting the needle without performing any steering manoeuvres. The second case calculates the future deflection of the needle assuming the user rotates the needle base around its shaft by 180 degrees at the current insertion depth. As both cases are displayed simultaneously to the user, the optimal depth at which the needle must be rotated in order to reach the target can be easily identified during the insertion process.

In the current configuration, the needle is connected to an existing needle insertion robot. This provides the user with a training environment where he can control the insertion robot actions, i.e., insertion depth and needle axial rotation, based on the provided visual feedback. If the user is manually inserting the needle, one simply needs to measure the position of the user's hand. This can be done in various different ways, including a wearable wristband with an embedded inertial measurement unit, or using additional optical trackers. Inserting the needle on the same side as the mirror can be done with only minor changes in the needle model.

The system is easy to implement, and is cost-effective. The added information supplied by this device allows the use to develop needle steering skills in either manual or robotic-assisted brachytherapy. Future efforts will focus on tracking the movements of implanted seeds to provide an accurate map of the seeds distribution and to evaluate the efficiency of the proposed system as a training environment for prostate brachytherapy.

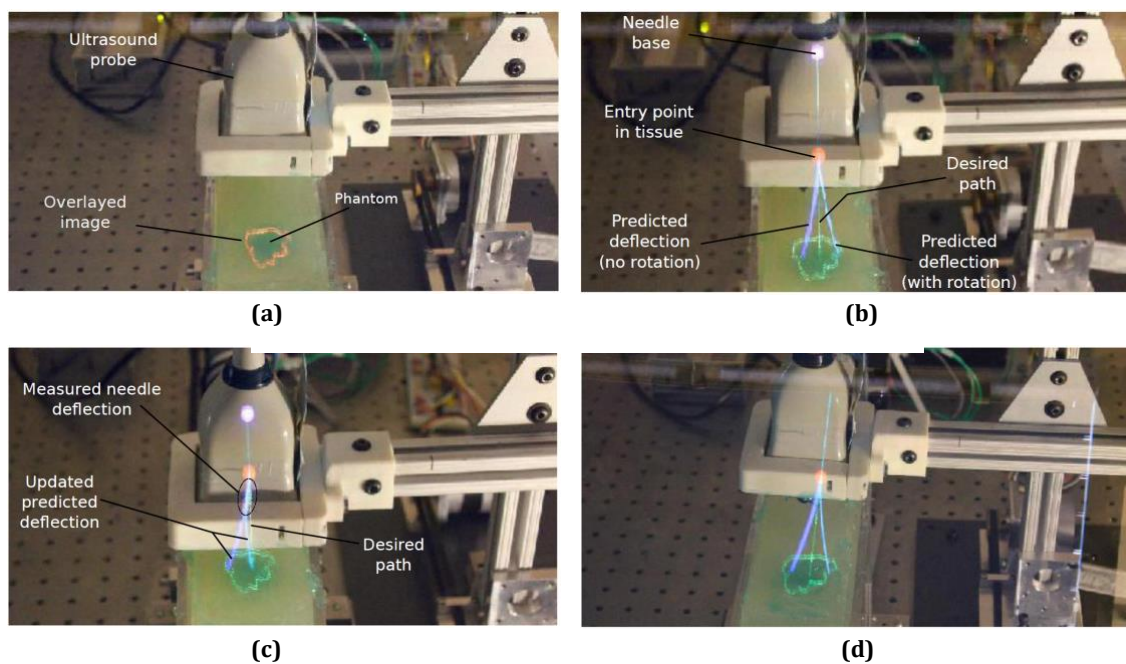


**Figure 7 - Images as seen by the user. In (a) a cross section of the phantom is shown in the plane that contains the needle. In (b) the needle is inserted by 5 mm in the tissue and the future deflections are calculated by the needle-tissue model. In (c) the needle is inserted to 40% of the maximum insertion depth and the estimated deflection is updated. In (d), the user moves his/her head to the right and the images are readjusted.**

## REFERENCES

Rossa (2017) - C. Rossa, and M. Tavakoli, "Issues in closed-loop needle steering," Control Engineering Practice, vol. 62, pp. 55-69, 2017, DOI: 10.1016/j.conengprac.2017.03.004.

Weiss (2011) - C. Weiss, D. Marker, G. Fischer, G. Fichtinger, A. Machado, and J. Carrino, "Augmented reality visualization using image overlay for MR-guided interventions: system description, feasibility, and initial evaluation in a spine phantom," American Journal of Roentgenology, vol. 196, no. 3, pp. W305-W307, 2011.

Nikou (2000) - C. Nikou, A. M. Digioia, M. Blackwell, B. Jaramaz, and T. Kanade, "Augmented reality imaging technology for orthopaedic surgery," *Operative Techniques in Orthopaedics*, vol. 10, no. 1, pp. 82–86, 2000.

Blackwell (2000) - M. Blackwell, C. Nikou, A. DiGioia, and T. Kanade, "An image overlay system for medical data visualization," *Medical Image Analysis*, vol. 4, no. 1, pp. 67–72, 2000.

Fichtinger (2005) - G. Fichtinger, A. Deguet, K. Masamune, E. Balogh, G. Fischer, H. Mathieu, R. Taylor, S. Zinreich, and L. Fayad, "Image overlay guidance for needle insertion in CT scanner," *Biomedical Engineering, IEEE Transactions on*, vol. 52, no. 8, pp. 1415–1424, Aug 2005.

Westwood (2006) - J. Westwood et al., "MRI image overlay: applications to arthrography needle insertion," *Medicine Meets Virtual Reality 14: Accelerating Change in Healthcare: Next Medical Toolkit*, vol. 119, p. 150, 2006.

Magee (2007) - D. Magee, Y. Zhu, R. Ratnalingam, P. Gardner, and D. Kessel, "An augmented reality simulator for ultrasound guided needle placement training," *Medical & biological engineering & computing*, vol. 45, no. 10, pp. 957–967, 2007.

Zhu (2006) - Y. Zhu, D. Magee, R. Ratnalingam, and D. Kessel, "A virtual ultrasound imaging system for the simulation of ultrasound-guided needle insertion procedures," in *Proceedings of Medical Image Understanding and Analysis*, pp. 61–65, 2006.

Wacker (2005) - S. Nicolau, L. Soler, D. Mutter, and J. Marescaux, "Augmented reality in laparoscopic surgical oncology," *Surgical oncology*, vol. 20, no. 3, pp. 189–201, 2011.

Wacker (2006) - F. Wacker, S. Vogt, A. Khamene, J. Jesberger, S. Nour, D. Elgort, F. Sauer, J. Duerk, and J. Lewin, "An augmented reality system for MR image-guided needle biopsy: Initial results in a swine model 1," *Radiology*, vol. 238, no. 2, pp. 497–504, 2006.

Nicolau (2005) - S. Nicolau, X. Pennec, L. Soler, and N. Ayache, "A complete augmented reality guidance system for liver punctures: First clinical evaluation," in *Medical Image Computing and Computer-Assisted Intervention, MICCAI*. Springer, pp. 539–547, 2005.

Nicolau (2009) - S. Nicolau, X. Pennec, L. Soler, X. Buy, A. Gangi, N. Ayache, and J. Marescaux, "An augmented reality system for liver thermal ablation: design and evaluation on clinical cases," *Medical Image Analysis*, vol. 13, no. 3, pp. 494–506, 2009.

Teber (2009) - D. Teber, S. Guven, T. Simpfendörfer, M. Baumhauer, E. Güven, F. Yencilek, A. Gözen, and J. Rassweiler, "Augmented reality: a new tool to improve surgical accuracy during laparoscopic partial nephrectomy? Preliminary in vitro and in vivo results," *European Urology*, vol. 56, no. 2, pp. 332–338, 2009.

Stetten (2001) - G. Stetten and V. Chib, "Overlaying ultrasonographic images on direct vision." *Journal of Ultrasound in Medicine*, vol. 20, no. 3, pp. 235–240, 2001.

Stetten (2001b) - G. Stetten, V. Chib, D. Hildebrand, and J. Bursee, "Real time tomographic reflection: phantoms for calibration and biopsy," in *Augmented Reality, 2001. Proceedings. IEEE and ACM International Symposium on*, pp. 11–19, 2001.

Sauer (2002) - F. Sauer, A. Khamene, and S. Vogt, "An augmented reality navigation system with a single-camera tracker: System design and needle biopsy phantom trial," in *Medical Image Computing and Computer-Assisted Intervention - MICCAI Springer*, pp. 116–124, 2002.

Fischer (2007) - G. Fischer, A. Deguet, C. Csoma, R. H. Taylor, L. Fayad, J. A. Carrino, S. J. Zinreich, and G. Fichtinger, "Mri image overlay: application to arthrography needle insertion," *Computer Aided Surgery*, vol. 12, no. 1, pp. 2–14, 2007.

Rossa (2016) - C. Rossa, M. Khadem, R. Sloboda, N. Usmani, and M. Tavakoli, "Adaptive quasi-static modelling of needle deflection during steering in soft tissue," *IEEE Robotics and Automation Letters*, vol. PP, no. 99, pp. 1–1, 2016.

Zhao (2012) - Y. Zhao, H. Liebgott, and C. Cachard, "Tracking micro tool in a dynamic 3D ultrasound situation using kalman filter and ransac algorithm," in *Biomedical Imaging (ISBI), IEEE International Symposium on. IEEE*, pp. 1076–1079, 2012.